

## MIT Open Access Articles

*Buckling-induced encapsulation of  
structured elastic shells under pressure*

The MIT Faculty has made this article openly available. **Please share** how this access benefits you. Your story matters.

**Citation:** Shim, J., C. Perdigou, E. R. Chen, K. Bertoldi, and P. M. Reis. "Buckling-Induced Encapsulation of Structured Elastic Shells Under Pressure." *Proceedings of the National Academy of Sciences* 109, no. 16 (March 26, 2012): 5978–5983.

**As Published:** <http://dx.doi.org/10.1073/pnas.1115674109>

**Publisher:** National Academy of Sciences (U.S.)

**Persistent URL:** <http://hdl.handle.net/1721.1/89828>

**Version:** Final published version: final published article, as it appeared in a journal, conference proceedings, or other formally published context

**Terms of Use:** Article is made available in accordance with the publisher's policy and may be subject to US copyright law. Please refer to the publisher's site for terms of use.



# Buckling-induced encapsulation of structured elastic shells under pressure

Jongmin Shim<sup>a,1</sup>, Claude Perdigo<sup>b</sup>, Elizabeth R. Chen<sup>c</sup>, Katia Bertoldi<sup>a,1,2</sup>, and Pedro M. Reis<sup>b,1,2</sup>

<sup>a</sup>School of Engineering and Applied Sciences, Harvard University, Cambridge, MA 021383; <sup>b</sup>Departments of Mechanical Engineering and Civil and Environmental Engineering, Massachusetts Institute of Technology, Cambridge, MA 02139; and <sup>c</sup>Department of Mathematics, University of Michigan, Ann Arbor, MI 48109

Edited by\* John W. Hutchinson, Harvard University, Cambridge, MA, and approved January 9, 2012 (received for review September 22, 2011)

**We introduce a class of continuum shell structures, the Buckliball, which undergoes a structural transformation induced by buckling under pressure loading. The geometry of the Buckliball comprises a spherical shell patterned with a regular array of circular voids. In order for the pattern transformation to be induced by buckling, the possible number and arrangement of these voids are found to be restricted to five specific configurations. Below a critical internal pressure, the narrow ligaments between the voids buckle, leading to a cooperative buckling cascade of the skeleton of the ball. This ligament buckling leads to closure of the voids and a reduction of the total volume of the shell by up to 54%, while remaining spherical, thereby opening the possibility of encapsulation. We use a combination of precision desktop-scale experiments, finite element simulations, and scaling analyses to explore the underlying mechanics of these foldable structures, finding excellent qualitative and quantitative agreement. Given that this folding mechanism is induced by a mechanical instability, our Buckliball opens the possibility for reversible encapsulation, over a wide range of length scales.**

Jitterbug | deployable structure

Advances in fabrication technology are enabling functional origami-like structures at the nano- and microscales (1–3), including encapsulation using hollow shell structures (4–7). In engineering, these structures are receiving increasing attention for their promising role as vehicles for drug delivery (8), material synthesis agents (9), optical devices (10), and sensors (11). An interesting avenue is the introduction of gating (also known as actuation) mechanisms into such capsules by incorporating functional elements into their structural layout toward tunable encapsulation. Coupling conventional actuation mechanisms at the microscale (including electromagnetic, piezoelectric, thermal, electrochemical, rheological) with buckling may lead to unique or more efficient functional modes of deformation (12, 13). As an example, the Venus flytrap combines a swelling mechanism with buckling behavior to increase the speed of leaf motility (14, 15). Also, an active microhydrogel device was recently designed for dynamic actuation using a swelling-induced elastic instability (16).

There are a few existing hollow shell structures which have gating mechanisms, albeit not driven by buckling. Viruses are an ubiquitous class of such examples in nature. Their capsids possess a spherical shell structure that encloses and transports viral nucleic acids (17, 18) and can undergo reversible structural transformations by which gated holes can open or close under pH changes (18). This transformation occurs due to the expansion of the vertices of the truncated icosahedral structure of the virus, resulting in 60 hole openings. Using this deployable capability, viruses have been used as protein cages for encapsulation (19). In order to describe the virus swelling/shrinking behavior, Kovács et al. investigated the possible geometric compatibility with polyhedral models (20, 21).

The Jitterbug, introduced by R. Buckminster Fuller in the 1960s, is another example of a hollow shell structure satisfying geometric compatibility for gating holes. It enables the morphing

between an octahedron and a cuboctahedron (22), thereby imparting flexibility to otherwise rigid grid structures. Since then, a number of studies have generalized the understanding of Jitterbug-like motion (face rotations at the vertices) through polyhedral transformations (23–25). These provide a robust set of rules for the design of spherical deployable structures that can fully close into their collapsed state. A popular commercial toy, Hoberman's Twist-o (Hoberman Associates) (26) which comprises a rigid network of struts connected by rotating hinges (Fig. 1A), also morphs from an open grid shell into a collapsed configuration. One drawback of these configurations toward practical applications is that the deformation is localized at the vertices of the polyhedra and a large number of hinges and rotating elements is required to achieve the intended motion.

Here, motivated by these opportunities for augmented motion and deformation of structures, we explore buckling as a possible gating mechanism for structured spherical shells. Our shells are patterned with a regular array of circular voids and loaded by reducing the internal pressure. Below a critical pressure, the narrow ligaments between the voids buckle, leading to a cooperative buckling cascade of the skeleton of the ball. We exploit this pattern transformation that leads to closure of all the holes, which is analogous to a structural negative Poisson's ratio effect previously studied in two dimensions (27), but now on a three-dimensional structure. Because our patterned shell has a geometry reminiscent of a buckyball (28) and, moreover, it can be activated by buckling, we name it the Buckliball. We first show the results of a combination of desktop-scaled experiments (Fig. 1B) and finite element (FE) simulations (Fig. 1C) on encapsulation through pressure-induced buckling of spherical shells. For the sake of experimental convenience and accurate control, we choose pressure as the actuation mechanism for the Buckliball. Consequently, thin membranes covering the holes are introduced in our samples to enable us to readily load the structure. Because the numerical results reveal that the characteristic deformation modes are only marginally affected by the presence of the membranes, for the sake of generality we then focus on the skeleton of the Buckliball without membranes over the voids and identify the underlying mechanical ingredients. Finally, through a scaling analysis, we provide a master curve for design guidelines of this class of structures.

## Experimental Results

Inspired by the construction and motion of the rigid toy in Fig. 1A, we have made use of rapid prototyping techniques to fabricate a continuum version of the spherical grid shell made of a soft

Author contributions: J.S., K.B., and P.M.R. designed research; J.S., C.P., E.R.C., K.B., and P.M.R. performed research; J.S. analyzed data; and J.S., K.B., and P.M.R. wrote the paper.

The authors declare no conflict of interest.

\*This Direct Submission article had a prearranged editor.

<sup>1</sup>J.S., K.B., and P.M.R. contributed equally to this work.

<sup>2</sup>To whom correspondence may be addressed. E-mail: bertoldi@seas.harvard.edu and preis@mit.edu.

This article contains supporting information online at [www.pnas.org/lookup/suppl/doi:10.1073/pnas.1115674109/-DCSupplemental](http://www.pnas.org/lookup/suppl/doi:10.1073/pnas.1115674109/-DCSupplemental).





the proposed spherical shells have two dimensionless design parameters: the ratio of the shell thickness to the inner radius,

$$\tau = \frac{t}{R_i}, \quad [1]$$

and the ratio of the void volume to the intact shell volume,

$$\psi = \frac{N}{2} \left[ 1 - \cos\left(\frac{\phi - \alpha}{2}\right) \right], \quad [2]$$

where  $N$  is the number of holes for the corresponding polyhedron,  $\alpha$  is the angle which defines the narrowest width of the ligament, and  $\phi$  is the angle between two vectors that originate at the shell center and terminate at two neighboring vertices of a folded polyhedron (see Fig. 4 A and B). Because the void's center in the expanded polyhedron is placed at the vertex locations of the folded polyhedron,  $\phi$  also represents the angle relating the center-to-center distance between two adjacent circular voids in the expanded polyhedron (see *SI Text* for details). Note that both  $N$  and  $\phi$  are fixed for a particular hole configuration and the possible pairs for the five configurations mentioned above are  $\langle N, \phi \rangle = \langle 6, \frac{\pi}{2} \rangle$ ,  $\langle 12, \frac{\pi}{3} \rangle$ ,  $\langle 24, \cos^{-1}\left(\frac{3+2\sqrt{2}}{5+2\sqrt{2}}\right) \rangle$ ,  $\langle 30, \frac{\pi}{5} \rangle$ , and  $\langle 60, \cos^{-1}\left(\frac{9+4\sqrt{5}}{11+4\sqrt{5}}\right) \rangle$ . The two additional design parameters  $\langle \tau, \psi \rangle$  prescribe the dimensions of the narrow ligaments which undergo buckling, thereby setting the threshold of the activation.

As observed in the experiments, the narrowest cross-section of ligament in the expanded status of the spherical shells governs the behavior of the on-sphere buckling of the ball. For this on-sphere buckling to happen, the second moment of area along the radial axis should be smaller than that along the perpendicular axis—i.e.,  $I_{rr} \leq I_{\theta\theta}$  (see Fig. 4B). The dimension of the narrowest cross-section of ligament is determined by  $\tau$  and  $\alpha$ , so that the restricting condition on the second moment of area reads

$$\frac{(\tau^2 + 3\tau + 3)^2}{(\tau + 2)^2(\tau^2 + 2\tau + 2)} = \frac{9\alpha \sin \alpha}{16(1 - \cos \alpha)}, \quad [3]$$

where  $\alpha$  is given by Eq. 2. Together, Eqs. 2 and 3 provide a relation between the two design parameters  $\langle \tau, \psi \rangle$ , which is set by the particular hole arrangement alone—i.e.,  $\langle N, \phi \rangle$ . As examples, in Fig. 4 C and D, we plot (dotted marked line) the design boundary set by Eqs. 2 and 3 for the spherical shells with 12 and 24 holes, respectively. Above this line, the Buckliballs are activated through the intended on-sphere buckling mode, whereas below it, other out-of-sphere (snap) buckling modes occur.

**Comparison with FE Simulations.** To assess our predictions on the effect of the hole arrangement and design parameters on ligament buckling, we perform a parametric study using FE simulations for the buckling analysis. FE models of the initially expanded spherical shells, for the five possible hole arrangements, are presented in Fig. 3B, to which an inward pressure is applied. For all five configurations, we perform a series of FE simulations on the design parameters  $\langle \tau, \psi \rangle$ . Representative results for shells with 12 and 24 holes are presented in Fig. 4 C and D as contour maps. In these phase diagrams, regions where out-of-sphere (snap) buckling occurs are represented in white. In the shaded regions where encapsulation (i.e., on-sphere buckling) occurs, the color in the contour plots represents the associated critical buckling pressure for onset of on-sphere buckling (normalized by the Young's modulus  $E$ ), given by the adjacent color bar. Representative examples of the calculated final on-sphere buckled shapes for all five possible arrangements on the folded status are also presented in Fig. 3D.

For a given hole configuration, this parametric study reveals that thicker shells and higher void volume fraction are preferable to make the Buckliball buckle on sphere. We highlight that the contour map boundary between the regions of on-sphere and out-of-sphere buckling is in good agreement with our criterion of design parameters (dashed marked line) based on the second

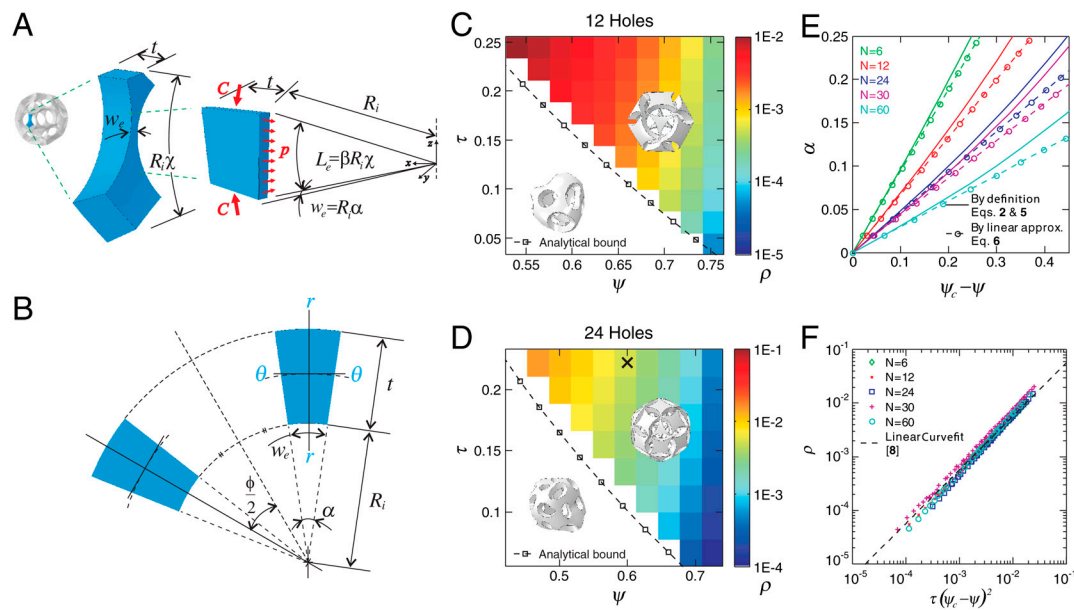


**Fig. 4.** (A) Representative ligament (Center) extracted from the Buckliball, and a simplified curved column model (Right). (B) Narrowest cross-section of the ligament. (C and D) Phase diagram of the two design parameters  $\langle \tau = t/R_i, \psi \rangle$ . The color-shaded region indicates on-sphere buckling and the white region represents the out-of-sphere buckling. The magnitude of the critical pressure for the onset of the on-sphere buckling is shown as a contour map with the adjacent color bar; (C) for 12 holes and (D) for 24 holes. The dotted marked lines indicate the analytical criterion from Eq. 3, based on the second moment of area. (E) Linear approximation of the normalized effective width of the ligament ( $\alpha = w_e/R_i$ , see [8]) in terms of effective solid volume fraction ( $\psi_c - \psi$ ). This linear approximation is valid up to the width ratio of  $\alpha \approx 0.15$ . (F) Master curve obtained from the buckling of the simplified ligament shapes. Regardless of the hole arrangements, the normalized critical pressure ( $\rho = p/E$ ) for the onset of on-sphere buckling has a distinctive relation with the two design variables  $\langle \tau, \psi \rangle$ ,  $\rho \approx A\tau(\psi_c - \psi)^2$ , with the prefactor  $A = 0.556$  and a coefficient of determination of  $\mathcal{R}^2 = 0.998$ .

moment of area of the narrowest cross-section of the ligaments. Because our criterion does not consider the ligament curvature (which can favor the out-of-sphere buckling), it may provide a slightly less conservative design space of the buckling for encapsulation, which is, nonetheless, still in good agreement with the FE simulation results.

In addition, we explored the effect of geometric defects (unavoidable during fabrication) and performed an additional set of simulations accounting for imperfections, as summarized in the *SI Text*. These simulations demonstrate that the on-sphere buckling of the Buckliball leading to the desired encapsulation feature is robust and not affected by moderate levels of imperfections.

### Design Master Curve for Encapsulation

We now provide a single master curve for the rational design of the Buckliball toward encapsulation applications. Thus far we have shown that, despite their complex overall geometry, the behavior of our Buckliballs is primarily governed by the geometry of the narrow ligaments of the shell. We proceed by considering the narrowest part of the ligament shown in Fig. 4A. Using the force equilibrium at each individual ligament, we can obtain an approximate relation between the compressive load  $C$  acting on its two ends and the pressure  $p$  applied to its inner surface,

$$C \approx R_i^2 \alpha p, \quad [4]$$

which is valid for small values of  $\alpha$  (i.e., large porosity) because we employ the linear approximation  $\sin \alpha \approx \alpha$  (see *SI Text* for derivation).

To simplify our analysis, the shape of the selected part of the narrow ligament is further approximated by a curved column with dimensions  $t$ ,  $L_e$ , and  $w_e$  (see schematic diagram in Fig. 4A). Here, the effective width of the ligament ( $w_e$ ) and the effective column length ( $L_e$ ) are defined as

$$w_e = R_i \alpha \quad \text{and} \quad L_e = \beta R_i \chi, \quad [5]$$

where  $\chi$  is the angle between two vectors which originate at the shell center and terminate at the center of the two neighboring solid parts of an expanded polyhedron (see Fig. 4A), and  $\beta \in (0, 1]$  is a prefactor relating the ligament length to the effective column length. Note that the angle  $\chi$  is fixed for a particular hole configuration. The possible pairs  $\langle N, \chi \rangle$  for the five configurations are  $\langle 6, \cos^{-1}(\frac{1}{3}) \rangle$ ,  $\langle 12, \cos^{-1}(\frac{1}{\sqrt{3}}) \rangle$ ,  $\langle 24, \frac{\pi}{4} \text{ and } \cos^{-1}(\sqrt{\frac{2}{3}}) \rangle$ ,  $\langle 30, \cos^{-1}(\sqrt{\frac{5+2\sqrt{5}}{15}}) \rangle$ , and  $\langle 60, \cos^{-1}(\sqrt{\frac{3+\sqrt{5}}{6}}) \text{ and } \cos^{-1}(\sqrt{\frac{5+\sqrt{5}}{10}}) \rangle$  reflecting that Buckliballs with 24 and 60 holes have two types of ligaments with slightly different lengths. Substituting  $w_e$  and  $L_e$  (Eq. 5) into Euler's buckling equation for a single ligament yields

$$C_{cr} = \frac{\pi^2 E t w_e^3}{12 L_e^2} \approx \frac{\pi^2 E t R_i^3 \alpha^3}{12 \beta^2 \chi^2}. \quad [6]$$

Combining this critical buckling load for a single ligament (Eq. 6) with the pressure-induced compressive load applied to the ligaments (Eq. 4), we obtain an expression for the normalized buckling pressure (denoted by  $\rho = p_{cr}/E$ ) in terms of  $\tau$  and  $\alpha$ ,

$$\rho \approx \frac{\pi^2}{12 \beta^2 \chi^2} \tau \alpha^2. \quad [7]$$

The angle  $\alpha$  defining the narrowest width of the ligament is a nonlinear function of void volume fraction  $\psi$ , as shown in Eq. 2, which upon Taylor's series expansion allows us to express the angle  $\alpha$  as a linear function of  $\psi$  near  $\psi_c$ :

$$\alpha \approx \frac{2}{\sqrt{\psi_c(N - \psi_c)}} (\psi_c - \psi), \quad [8]$$

where  $\psi_c$  denotes a critical void volume fraction, beyond which the narrowest thickness of the ligaments vanishes (i.e.,  $\alpha = 0$  in Eq. 2) and the spherical shell loses structural integrity. The specific hole arrangement, alone, sets the value of  $\psi_c$  (see Eq. 2). In Fig. 4E we plot the angle  $\alpha$  as a function of  $(\psi_c - \psi)$ , which confirms the validity of the linear approximation in [8] for structures characterized by large values of porosity (i.e., small  $\alpha$ ).

Finally, substituting [8] into [7] provides a relation between the normalized buckling pressure  $\rho$  and the two design parameters  $\tau$  and  $\psi$ ,

$$\rho \approx A \tau (\psi_c - \psi)^2, \quad [9]$$

where the coefficient  $A = \pi^2 [3\beta^2 \chi^2 \psi_c (N - \psi_c)]^{-1}$  is a weak function of hole arrangement. In Fig. 4F we plot  $\rho$  versus  $A(\psi_c - \psi)^2$  for all of the numerical runs (over 250) from the five hole configurations, including the previous parametric study (Fig. 4C and D). All of the data collapse onto a linear master curve with a prefactor of  $A = 0.556$  (coefficient of determination  $\mathcal{R}^2 = 0.998$ ), which confirms our predictions in [9]. In addition, from the identified value of the prefactor  $A$ , we can inversely calculate the prefactor  $\beta$  for all the five hole configurations, finding that its mean value is  $\langle \beta \rangle = 0.839$ .

Despite the a priori complex geometry of the Buckliball, this master curve indicates that, regardless of the hole arrangement, the encapsulation behavior of the ball is indeed dictated by the buckling of ligaments of the shells. Our analysis provides us with two practical guidelines for the design of the Buckliball. The first (Eq. 3 shown in Fig. 4C and D) sets the shell dimensions required for buckling-induced encapsulation. Secondly, the master curve ([9] shown in Fig. 4F) provides an estimation for the critical buckling pressure for actuation of the Buckliball with given dimensions and for a particular hole arrangement. During this design procedure, the fabrication constraint can be explored by checking the smallest dimension of the ball, which is the narrowest cross-section of ligament ([8] shown in Fig. 4E) for the given porosity and hole arrangement.

### Conclusion

We have introduced the Buckliball, a class of continuum elastic shells structures, which exhibits encapsulation through folding that is induced by buckling under pressure loading. An important advantage of our system is that it is made of a single continuum structure, which eliminates the need for a large number of hinges and rotating elements required in typical foldable/deployable structures. We chose pressure as the actuation mechanism and concentrated on macroscopic length scales for the sake of experimental convenience and accurate control. We then focused our analysis on the loading of the Buckliball's skeleton without membranes to aim for further generality of the results.

Our combined experimental, numerical, and theoretical approach allowed us to rationalize the underlying mechanical ingredients and yielded a series of simple design guidelines, including a master curve, for buckling-induced encapsulation. Moreover, because the folding mechanism exploits a mechanical instability that is general, our study raises the possibility for reversible, tunable, and controllable encapsulation, over a wide range of length scales. Recent developments in microscale fabrication open exciting opportunities for miniaturization of the Buckliball, for example, using projection microstereo lithography (33) or galvanic exchange-coupled Kirkendall growth (34) to produce patterned hollow particles. Our study therefore opens avenues for encapsulation at the microscale using other forms of loading, such as bilayer structures (e.g., unshrinkable outer ball attached to shrinkable inner ball) having swelling/shrinking actuation



# Supporting Information

Shim et al. 10.1073/pnas.1115674109

## SI Text

**Derivation of Equation for Void-Volume Fraction, Eq. 2.** To clarify the derivation of Eq. 2 in the main manuscript, we focus on the simplest case of the Buckliball with six voids (Fig. S1), although the argument is general and applicable to all other four configurations.

We start by deriving the relation between the angles ( $\phi$ ,  $\theta$  and  $\alpha$ ) used in Eq. 2 of the main manuscript. We define  $\phi$  as the angle between two vectors, which originate at the shell center and terminate at two neighboring vertices of a folded polyhedron (see the schematic diagram in Fig. S1A). Because the void's center in the expanded polyhedron (i.e., cuboctahedron for this specific case) is placed at the vertex locations of the folded polyhedron (i.e., octahedron for this specific case),  $\phi$  also represents the angle relating the center-to-center distance between two adjacent circular voids in the expanded polyhedron. In addition, we define  $\alpha$  as the angle that sets the narrowest width of the ligament (Fig. S1B), and  $\theta$  as the angle that sets the diameter of the void (Fig. S1B). From geometry, we obtain

$$\theta = \phi - \alpha. \quad [\text{S1}]$$

Secondly, we calculate the volume of the intact spherical shell:

$$V_{\text{shell}} = \frac{4}{3}\pi[R_o^3 - R_i^3], \quad [\text{S2}]$$

where  $R_i$  and  $R_o$  denote the inner and outer radius of the shell, respectively.

We now need to calculate the volume of a single void on the spherical shell (Fig. S1D). Because each void is defined by a cone of opening angle  $\theta$  and vertex located at the center of the sphere (Fig. S1C), its volume is given by

$$V_{\text{void}} = \frac{2}{3}\pi[R_o^3 - R_i^3] \left[ 1 - \cos\left(\frac{\theta}{2}\right) \right]. \quad [\text{S3}]$$

Finally, combining Eqs. S1–S3, we obtain the following expression for the void-volume-fraction,

$$\psi = \frac{NV_{\text{void}}}{V_{\text{shell}}} = \frac{N}{2} \left[ 1 - \cos\left(\frac{\phi - \alpha}{2}\right) \right], \quad [\text{S4}]$$

which corresponds to Eq. 2 in the main manuscript.

**Phase Diagrams of Design Parameters  $\langle \tau, \psi \rangle$ .** We present additional phase diagrams of design parameters for shells with 6, 30, and 60 holes, which are not included in Fig. 4 of the main manuscript because of the page limitation.

Because the experiments suggest that the narrowest cross-section of ligament in the expanded status of the spherical shells governs the on-sphere buckling behavior of the balls, by comparing the second moment of area along two axes (i.e.,  $I_{rr} \leq I_{\theta\theta}$ ) we obtain a relation between the two design parameters  $\langle \tau, \psi \rangle$  (Eqs. 2 and 3 in the main manuscript). The corresponding phase boundary is plotted as a marked line in Fig. S2. In addition, to assess our predictions, we perform a series of finite element simulations where we investigate the buckling of Buckliball characterized by different pairs of the design parameters  $\langle \tau, \psi \rangle$ . The phase diagrams for shells with 6, 30, and 60 holes are presented in Fig. S2. In these phase diagrams, regions where out-of-sphere (snap) buckling occurs are represented in white. In the shaded regions

where encapsulation (i.e., on-sphere buckling) occurs, the color in the contour plots represents the associated critical buckling pressure for onset of on-sphere buckling (normalized by the Young's modulus  $E$ ), given by the adjacent color bar. We find that the contour map boundary between the regions of on-sphere and out-of-sphere buckling is in good agreement with our analytical prediction based on the second moment of area of the narrowest cross-section of ligament.

**Derivation of Equation for Pressure-Compression Relation, [4].** We proceed by presenting a detailed derivation of the scaling in [4] in the main manuscript (Eq. [8] in this document). We start by considering a single ligament and simplify its geometrical description using a curved column with uniform width ( $w_e = R_i\alpha$ ) and effective column length ( $L_e = \beta R_i\chi$ ) (Fig. S3). In the main manuscript, [4] can be obtained from the force equilibrium along the radial direction for the simplified curved column. To simplify the derivation, let's orient the column so that the radial direction at the center of its width coincides with the  $x$  axis of the Cartesian coordinate (see Fig. S3, *Right*). Introducing a spherical coordinate system ( $r > 0$ ,  $\theta \in [0, \pi]$ ,  $\varphi \in [0, 2\pi)$ ) so that  $x = r \sin \theta \cos \varphi$ ,  $y = r \sin \theta \sin \varphi$ , and  $z = r \cos \theta$ , the component along the  $x$  direction (i.e., the radial direction) of the pressure  $p$ , denoted by  $F_x^p$ , can be obtained as

$$\begin{aligned} F_x^p &\approx \int_{\theta=\frac{\pi}{2}-\frac{\alpha}{2}}^{\theta=\frac{\pi}{2}+\frac{\alpha}{2}} \int_{\varphi=-\frac{\beta\chi}{2}}^{\varphi=\frac{\beta\chi}{2}} (p \sin \theta \cos \varphi) R_i^2 \sin \theta d\theta d\varphi \\ &\approx p R_i^2 [\alpha + \sin \alpha] \sin\left(\frac{\beta\chi}{2}\right). \end{aligned} \quad [\text{S5}]$$

Because the component along the  $x$  direction of the compressive force  $C$ , denoted by  $F_x^C$ , is given by

$$F_x^C = 2C \sin\left(\frac{\beta\chi}{2}\right), \quad [\text{S6}]$$

force equilibrium in the  $x$  direction (i.e.,  $F_x^p = F_x^C$ ) yields

$$p R_i^2 [\alpha + \sin \alpha] = 2C. \quad [\text{S7}]$$

For large values of porosity  $\alpha \rightarrow 0$ , so that we can use the approximation  $\sin \alpha \approx \alpha$ , and Eq. S7 reduces to

$$C \approx R_i^2 \alpha p, \quad [\text{S8}]$$

which corresponds to [4] in the main manuscript.

**Postbuckling Analysis: Finite Element Simulations.** Because the buckling analysis performed using Abaqus/Standar solver reveals that linear continuum elements lead to strong mesh-size dependent behavior, we built all the models using quadratic continuum elements (C3D10MH: a quadratic hybrid-continuum element with a 10-node modified tetrahedron having one additional variable relating to pressure) for both the thin membranes and the skeleton (thicker parts) of the shells.

Note that continuum elements are also used for the membrane, to resolve issues of compatibility between the quadratic continuum elements and linear shell elements for large-strain formulations. Although Abaqus/Standard provides various conventional thin shell element types, only few shell elements are suitable for large-strain analysis (1); these are linear thin shell



element (e.g., S3(R), S4(R), etc.) and quadratic thick shell elements (e.g., SC8(R), etc.), which are also called continuum shell elements. Both element types have a compatibility issue with quadratic continuum element types of *C3D10M(H)* and therefore we decide to use continuum elements for both the thin membranes and the thicker parts of the shells.

To perform the postbuckling analysis under volume-controlled conditions, the Buckliball was modeled as a spherical shell filled with fluid for which we used hydrostatic fluid elements (F3D3 with a mesh sweeping seed size of 1.25 mm). The fluid has been assumed to be compressible air having a density of 1.024 kg/m<sup>3</sup> at 20 °C and its volume has been progressively reduced during the simulations. Because Abaqus/Standard provides only linear hydrostatic fluid elements (element type *F3D3*), the mesh for the fluid elements was designed such that four fluid elements (i.e., four *F3D3* elements) are attached to a single face of the quadratic solid element (i.e., *C3D10MH*). In addition, implicit dynamic analysis were performed using Newmark algorithm with  $\beta = 0.276$  and  $\gamma = 0.550$  (such conditions are achieved by setting  $\alpha = -0.05$ , “\*DYNAMIC, ALPHA = -0.05”). Note that this damping is purely numerical and is different from the material damping (2). The kinetic energy was monitored during simulations and observed to be less than 3.0% of the strain energy, ensuring quasi-static conditions.

A mesh sweeping seed size of 2.5 mm was chosen for the solid elements, resulting in hydrostatic fluid elements of size that is roughly half the size of the solid elements due to the above-mentioned mesh design procedure. For example, the model used for the postbuckling analysis of the Buckliball with membrane thickness  $h = 0.5$  mm has 15,469 *C3D10MH* elements and 8,704 *F3D3* elements (Fig. S4A). Fig. S4C shows the results of the postbuckling analysis performed under volume-controlled conditions, which are presented in the main manuscript. The computational cost of the simulation was remarkably high; a single postbuckling analysis under volume control took 40 h using 48 central processing units. This extremely high computational cost for the volume-control simulations hindered further investigation on the effect of mesh size and numerical damping parameter.

For the sake of computational convenience, the accuracy of the mesh used in the volume-control simulations was ascertained performing several simulations under pressure-controlled conditions, whose computational cost is found to be less than one-fifth of that of the volume-controlled simulations. Therefore, models with sweeping mesh sizes of up to 1.0 mm were built and tested (see Fig. S4B).

For the static analysis under pressure-controlled conditions, a stabilized scheme using artificial damping was employed because the postbuckling behavior of the Buckliball covered by a thin membrane is characterized by two different types of sequential unstable buckling events (i.e., local snap-buckling events in the thin membranes followed by a global buckling mode of the skeleton). Note that the Abaqus/Standard solver provides an automatic stabilization with artificial damping; where viscous forces of the form  $F_v = cM^*v$  are added to the global equilibrium equations; here,  $c$  is a damping factor,  $M^*$  is an artificial mass matrix calculated with unit density, and  $v$  is the nodal velocity vector. We choose an option where the damping factor  $c$  is determined in such a way that the dissipated energy for a given increment is 0.02% of the extrapolated strain energy, which is the default value by using the Abaqus keyword “\*STATIC, STABILIZE = 0.0002”. When we reduce the damping factor below 0.02%, the

simulation stops before capturing the local snap-buckling of membranes. Thus, the damping factor of 0.02% is the smallest value with which the numerical simulations were still able to capture the correct postbuckling behavior. More details on this automatic stabilization scheme are presented in ref. 3.

Comparison of the results from the volume-controlled simulations (with mesh sweeping size of 2.5 mm shown in Fig. S4C) and pressure-controlled simulations (with mesh sweeping size of 1.0 mm shown in Fig. S4D) shows good agreement in terms of initial linear response and critical buckling pressure. These results confirm that the mesh size used in the volume-controlled simulations is fine enough to accurately predict the onset of buckling and postbuckling behavior. Moreover, although the pressure-controlled simulations were unable to capture the experimentally observed softening that follows immediately after the onset of buckling, this feature was accurately predicted by the volume-controlled simulations.

**Effect of Geometric Imperfections.** We have performed an additional set of simulations to explore the imperfection sensitivity of buckling for the Buckliball, focusing on the Buckliball with 24 voids. The Buckliball had an inner radius  $R_i = 22.5$  mm, shell thickness  $t = 5$  mm, void-volume fraction  $\psi = 58.7\%$ , and the voids were not covered by a membrane. For this given Buckliball design, we introduced imperfections in the form of different void size and misplaced void location on the sphere when compared to their geometrically exact set by the underlying polyhedron. We explored the response of structures with stochastically displaced and sized voids of amplitude  $a = 1\%t, 5\%t, 10\%t, \text{ and } 15\%t$  (i.e.,  $t = 5$  mm). Note that, for imperfections of magnitude larger than 15% $t$ , the narrowest width of ligament vanishes so that the Buckliball loses structural integrity. Five configurations are generated and tested for each value of  $a$ , totaling 20 sets of simulations for both buckling and postbuckling analysis. The dependence of the critical buckling load as a function of  $a$  is presented in Fig. S5, showing that the critical pressure tends to decrease as the magnitude of imperfection increases. In addition, representative snapshots from the postbuckling analysis are shown in Fig. S6. For the cases with  $a = 1\%t$  and 5% $t$ , the pressure at the onset of buckling is found to be only marginally affected by imperfection (less than 1%) and all five configurations show a nearly perfect on-sphere buckling leading to the desired encapsulation behavior, and therefore only one representative snapshot is reported (Fig. S6A and B). On the other hand, various postbuckled shapes are observed for the cases of  $a = 10\%t$  and 15% $t$  and three representative snapshots are presented for each case (Fig. S6C and D). As the magnitude of imperfection increases, the width of the ligaments of the Buckliball is strongly affected by the imperfections, so that the deformation tends to localize within the narrowest ligaments. For  $a = 10\%t$ , all five Buckliballs show the desired encapsulation postbuckling behavior, albeit with postbuckled shapes that can deviate from a sphere (Fig. S6C). Moreover, the pressure at buckling is reduced by roughly 7%. Finally, for  $a = 15\%t$ , the imperfection is found to strongly affect the response of the structures so that only one configuration out of five shows an encapsulation postbuckling behavior (Fig. S6D) and the critical pressure is now reduced by approximately 15%.

This additional set of simulations demonstrates that the encapsulation mechanism of the Buckliballs is robust and not affected by geometric imperfections up to  $a = 10\%t$ .

1. Abaqus (2008) *Abaqus Analysis User's Manual, Ver 6.8* (Dassault Systèmes Simulia Corp., Providence, RI), Sect 28.6.  
2. Abaqus (2008) *Abaqus Theory Manual, Ver 6.8* (Dassault Systèmes Simulia Corp., Providence, RI), Sect 2.4.

3. Abaqus (2008) *Abaqus Analysis User's Manual, Ver 6.8* (Dassault Systèmes Simulia Corp., Providence, RI), Sect 7.1.



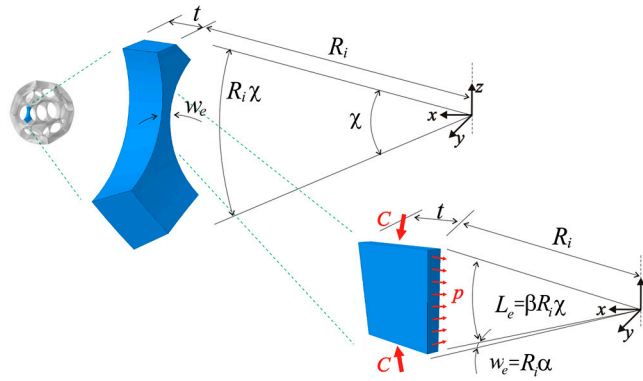


Fig. S3. Representative ligament extracted from the Buckliball and simplified curved column used in its buckling analysis.

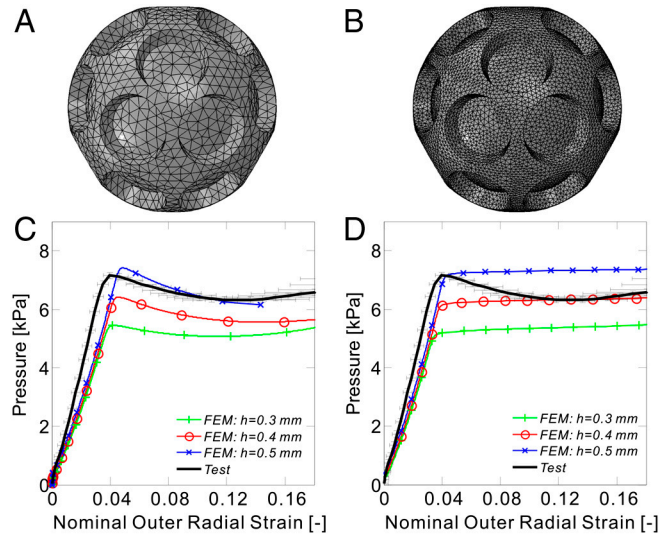


Fig. S4. (A and B) Meshed Buckliball with sweeping mesh size of (A) 2.5 mm and (B) 1.0 mm. (C and D) Dependence of the differential pressure of the ball on the nominal outer radial strain. Simulation results using finite element modeling (FEM), which are denoted by marked color lines, are obtained from (C) volume-controlled and (D) pressure-controlled conditions.

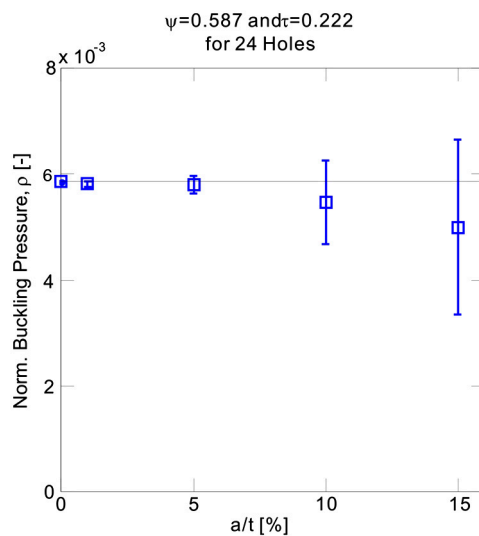


Fig. S5. Effect of imperfections on the normalized critical buckling pressure  $\rho = p/E$ . Blue square marks correspond to the mean value of five configurations and the size of error bar corresponds to the one-standard deviation. In addition, the black horizontal line represents the normalized critical buckling pressure for Buckliball without imperfections.

